Meas. Sci. Technol. 36 (2025) 095405 (10pp)

# Dynamic laboratory x-ray phase-contrast microtomography with structure-based prior regularisation

Harry Allan<sup>1,2,\*</sup>, Tom Partridge<sup>1</sup>, Joseph Jacob<sup>3,4</sup> and Marco Endrizzi<sup>1,2</sup>

- <sup>1</sup> Department of Medical Physics and Biomedical Engineering, University College London, London, United Kingdom
- <sup>2</sup> X-ray Microscopy and Tomography Laboratory, The Francis Crick Institute, London, United Kingdom
- <sup>3</sup> Hawkes Institute, University College London, London, United Kingdom
- <sup>4</sup> UCL Respiratory, University College London, London, United Kingdom

E-mail: harry.allan.21@ucl.ac.uk

Received 12 April 2025, revised 21 August 2025 Accepted for publication 2 September 2025 Published 11 September 2025



### **Abstract**

X-ray microtomography is a versatile tool allowing the measurement of the 3D structure of optically thick samples. As a non-destructive technique, it is readily adapted to 4D imaging, where a sample can be monitored over time, and especially in conjunction with the application of external stimuli. To apply this technique with the limited x-ray flux available at a conventional laboratory source, we leverage the contrast enhancement of free-space propagation phase-contrast imaging, achieving an increase in contrast-to-noise ratio (CNR) of 5.8x. Furthermore, we combine this with iterative reconstruction, using regularisation by a structure-based prior from a high-quality reference scan of the object. This combination of phase-contrast imaging and iterative reconstruction leads to a 29.2x improvement in CNR compared to the conventional reconstruction. This enables fully dynamic x-ray microtomography, with a temporal resolution of 9 s at a voxel size of 10.5 µm. We use this to measure the movement of a waterfront in the fine vessels of a wooden skewer, as a representative example of dynamic system evolving on the scale of tens of seconds.

Supplementary material for this article is available online

Keywords: x-ray phase-contrast, tomography, 4D imaging, iterative reconstruction

### 1. Introduction

The penetrating power of hard x-rays makes them a versatile tool for imaging the structure of non-transparent materials

\* Author to whom any correspondence should be addressed.

Original Content from this work may be used under the terms of the Creative Commons Attribution 4.0 licence. Any further distribution of this work must maintain attribution to the author(s) and the title of the work, journal citation and DOI.

across a range of length scales. In combination with tomography, this enables the reconstruction of 3D volumes and the recovery of complex internal sample morphology [1]. Being a non-destructive technique, x-ray tomography is readily extended to 4D (3 spatial + temporal dimension) imaging. This capability enables longitudinal in-situ testing of the same sample as it evolves with time, often examining the response of the test object to an external stimulus. Rather than acquiring separate 3D snapshots at intermediate time points, high temporal resolution systems allow fully dynamic imaging, in which data is continuously acquired while the test object evolves [2]. A range of fields have benefitted from *insitu* and dynamic x-ray tomography, including food science

[3, 4], additive manufacturing [5, 6], and biomedical sciences [7–9].

Achieving sufficient contrast-to-noise ratio (CNR) for tomographic reconstruction and subsequent analysis typically requires high x-ray flux to reduce scan times and enable the capture of fast dynamic processes. Specially designed synchrotron radiation facilities (SRFs) generate extremely bright x-ray beams by the acceleration of electron bunches. In addition to high x-ray flux, SRFs also deliver a coherent beam, allowing users to benefit from phase effects [10], rather than just x-ray attenuation. This enables the imaging of low-attenuation objects, and increases CNR compared to the equivalent attenuation only image [11]. These factors enable the highest temporal resolution at SRFs, with tomography acquisition times down to a few milliseconds [12–14].

Despite a growing number of facilities worldwide, the need for regular longitudinal access makes the development of dynamic x-ray tomography using laboratory x-ray sources an attractive prospect [15]. With peak x-ray brilliances (a measurement of the coherent flux) 6-10 orders of magnitude lower than those at SRFs, it is a challenge to obtain sufficient CNR for valuable analyses. Nevertheless, a number of demonstrations with temporal resolution on the order of 10 s [16–18], and even sub second [19–22] have been demonstrated. Similar to SRFs, x-ray phase-contrast imaging (XPCI) can also be employed at laboratory sources. A range of techniques have been developed to allow XPCI with their lower coherent flux by using optical elements in the beam [23-26]. These methods often provide the possibility for multi-contrast imaging, which can give unique insights into the sample, with dynamic applications in monitoring tissue freezing protocols [27] and in additive manufacturing [28]. However, these techniques often require multiple movements of optical elements, which complicates fast and dynamic imaging. Some techniques, particularly beam-tracking [25] and speckle-based imaging [26], can be set up to obtain multi-contrast (including phase) images with a 'single-shot'. However, the inclusion of optical elements still results in a decrease in x-ray flux, and single-shot modes typically also require a sacrifice in spatial sampling (and thus resolution).

It is for this reason that dynamic XPCI based on free-space propagation (FSP) [29] is particularly promising for lower brilliance sources. With this optics-less approach, the CNR boost of phase-contrast can be achieved with no loss of flux compared to the purely attenuation-based counterpart. It is interesting to note that the CNR improvement associated with XPCI is not constant with dose [11]. The CNR boost is more pronounced for shorter exposures, particularly with tomography, making XPCI an incredibly valuable tool for fast dynamic tomography. Outside of large-scale facilities, time-resolved FSP XPCI has been utilised for dynamic XPCI radiography of mouse lung motion using an inverse Compton scattering source [30]. Extending to 4D, regional lung function of a cystic fibrosis mouse model has been measured using a liquid metaljet source with a respiratory-gated acquisition [7].

A key development in the enabling of fast and dynamic tomography is the advancement of reconstruction algorithms. Compared to analytical methods, iterative algorithms [31]

such as the simultaneous iterative reconstruction technique [32] perform well with the undersampled and noisy projection data that are typical of dynamic imaging. Self-supervised deep learning methods such as noise2inverse [33] also offer promising results for handling noisy data, yet suffer when applied to undersampled data. Algorithms that utilise spatio-temporal [34] or structure-based [35] priors are particularly capable of generating useful reconstructions for time-resolved experiments, by exploiting mutual information between the target reconstruction and some other prior data.

We present dynamic x-ray microtomography with a laboratory source, achieving a temporal resolution of 9 s at a voxel size of  $10.5 \, \mu m$ . We demonstrate this through the measurement of water uptake in a birch wood skewer, proving quantitatively the CNR gain from applying XPCI to this low-attenuation material. Furthermore, to cope with the relatively low brilliance of the laboratory source, we apply a reconstruction method utilising a structure-based prior, to enable quality reconstruction from fast and undersampled datasets.

# 2. Methods

### 2.1. FSP XPCI

For x-rays passing through a thin, weakly refracting object, the near-field image intensity recorded by a detector downstream of the object is well described by Fresnel diffraction [36]. Thus, the intensity at the detector plane  $z = z_d$  can be approximated by the transport of intensity equation (TIE) as [29]

$$I(x,y,z=z_d) = \frac{I(x,y,z=z_o)}{M^2} \left( 1 - \frac{R_2 \lambda}{2\pi M} \nabla_{\perp}^2 \phi(x,y;\lambda) \right),$$
(1)

where  $R_2$  is the propagation distance from the object plane  $z = z_o$  to the detector plane,  $M = (R_1 + R_2)/R_1$  is the geometric magnification of the image (with  $R_1$  being the source-toobject distance),  $\lambda$  is the wavelength of the incident radiation, and  $\nabla^2 \phi(x, y; \lambda)$  is the transverse Laplacian of the objectinduced phase shift projected onto the xy-plane. It can therefore be shown that for  $R_2 = 0$ , the image recorded is simply the pure attenuation contact image  $I(x, y, z = z_o) = I(x, y, z = z_o)$ 0) exp  $\left(-\int_{\Omega} \mu(x,y,z;\lambda) dz\right)$ , where I(x,y,z=0) is the x-ray intensity in the absence of the object, and  $\int_{a} \mu(x,y,z;\lambda) dz$ is the integral along the beam path of the 3D distribution of the linear attenuation coefficient of the material. For a polychromatic x-ray source, as is typically used in laboratory imaging,  $I(x, y, z = z_d)$  is instead replaced by the weighted integral across  $\lambda$ . As the distance  $R_2$  is extended, the Laplacian term becomes significant and the image intensity becomes dependent not only on the amplitude of the wave at the object exit plane, but also on its phase. While in the near-field, the phase term grows linearly with increasing  $R_2$ . However, for finite xray source size and detector point spread function (PSF), the resultant measured image is given by the convolution of the total system PSF with the input image intensity, thus the fringe contrast depends also on the spatial resolution of the system.

Assuming that the detector PSF and the source spot are well described by Gaussian functions, the spatial resolution of the imaging system can be described by the total system PSF with width  $\sigma$  as

$$\sigma = \sqrt{\left(1 - \frac{1}{M}\right)^2 \sigma_{\rm s}^2 + \frac{\sigma_{\rm d}^2}{M^2}},\tag{2}$$

where  $\sigma_s$  is the width of the source spot distribution and  $\sigma_d$  is the width of the detector PSF. Thus it can be shown that for a fixed system length  $R_1 + R_2$ , there exists an optimum magnification  $M_{\rm opt}$  for which phase fringe contrast is maximised, by balancing the amplification of the Laplacian term and the system spatial resolution. This optimum is dependent only on the ratio of the source width and detector PSF [37, 38], and is given by

$$M_{\rm opt} = 1 + \frac{\sigma_{\rm d}}{\sigma_{\rm s}}. (3)$$

The dependence of the measured intensity on the system resolution makes it necessary to employ x-ray sources with some combination of small source spots [39] or high-resolution detectors [40] in order to make the phase fringes detectable.

Under the assumption of a monochromatic, paraxial, scalar x-ray field incident upon a homogenous object, the induced phase-shift may be retrieved from the mixed image as

$$\phi(x,y) = -\frac{1}{2} \frac{\delta}{\beta} \times \log \left( \left| \mathcal{F}^{-1} \left( \frac{\mathcal{F}(I(x,y,z=z_d)/I(x,y,z=0))}{\frac{\lambda R_2}{4\pi M} \frac{\delta}{\beta} (u^2 + v^2) + 1} \right) \right| \right),$$
(4

where  $\frac{\delta}{\beta}$  is the ratio of the real to imaginary parts of the object's complex refractive index,  $\mathcal{F}$  and  $\mathcal{F}^{-1}$  are the Fourier and inverse Fourier transform operators respectively, and (u,v) are the spatial frequency coordinates corresponding to the real space (x,y) detector pixel coordinates [41]. Violating the stated assumptions by replacing  $\lambda$  with the mean polychromatic wavelength  $\lambda_{\rm eff}$ , and applying the technique to real nonhomogenous objects, a high-contrast non-quantitative approximation of the phase-shift is retrieved.

# 2.2. Tomographic reconstruction

The aim of tomographic reconstruction is to solve the linear inverse problem

$$Au = b, (5)$$

where A is the x-ray forward projection operator, u is the volume to be recovered, and b is the measurement data [42]. For well-sampled and low-noise measurement data, analytical reconstruction based on methods such as the Feldkamp–Davis–Kress (FDK) algorithm [43] yields satisfactory reconstructions of u. For the reconstruction of noisy or undersampled data, analytical methods may not be sufficient, thus iterative methods become powerful alternatives.

In the case of dynamic x-ray tomography, it may be possible to obtain a high-quality reference scan of the sample before the initiation of the dynamic process. If the sample remains structurally similar to its initial state throughout the duration of the dynamic imaging, then the reconstruction  $\nu$  of the high quality reference can be used as a structure-based prior for regularisation of the iterative reconstruction [35, 44–46].

We justify this by considering some initial volume that transforms through some dynamic process into a new state, illustrated by the slices shown in figures 1(a) and (b). This could be representative of the filling of structures with a fluid, or changes in density of a structure. Despite containing some mutual information, there is no longer a 1:1 correspondence between the two states. To capture the existing mutual information, we examine the gradients of the two images. The resultant normalised direction of image gradients effectively captures this information, and is equal for both images, under the assumption that the shape of the structures remains constant. We quantify this for the illustrated example by the change in Pearson's correlation coefficient of 0.886 between the two images, versus 1.000 for their gradient directions.

It has been shown that this vectorial information can be harnessed to regularise certain inverse problems, by capturing this mutual information [47]. To apply this to tomography, we aim to solve the inverse problem

$$u(t) = \underset{u(t) \ge 0}{\operatorname{argmin}} \frac{1}{2} ||Au(t) - b||^2 + \alpha \, d\text{TV}\left(u(t), v\right), \quad (6)$$

where  $u(t) \ge 0$  enforces non-negativity of the solution of u at time t,  $\alpha$  controls the strength of the regularisation, and dTV(u(t),v) is the directional total variation regulariser, defined as [35]

$$dTV := ||D_{\nu}\nabla u(t)||_{2,1} = \sum_{x,y,z} (||D_{\nu}\nabla u(t)||_{2})_{x,y,z}.$$
 (7)

The weight matrix  $D_v$  captures the orthogonal components of the normalised gradient field  $\nabla v$ , incorporating a Tikhnonov regularisation parameter  $\eta$  to ensure numerical stability. Thus dTV regularisation encourages the solution to align with the edges and features present in the reference image v. To separately handle the smooth data fidelity term and the non-smooth dTV term, the inverse problem can be efficiently solved using the primal-dual hybrid gradient (PDHG) method.

#### 2.3. Experiments

The experiment was carried out at the National research facility for lab-based x-ray computed tomography (NXCT) multi-contrast x-ray micro-CT system [48], utilising a Rigaku MicroMax 007-HF rotating molybdenum anode x-ray source. The source was operated at  $50\,\mathrm{kV}$  tube voltage and  $24\,\mathrm{mA}$  current, without additional filtration. A custom detector based on a scintillator and lens-coupled sCMOS camera with a pixel size of  $15\,\mathrm{\mu m}$  was placed at a total distance  $R_1+R_2=460\,\mathrm{mm}$  away from the source. For a source of effective width

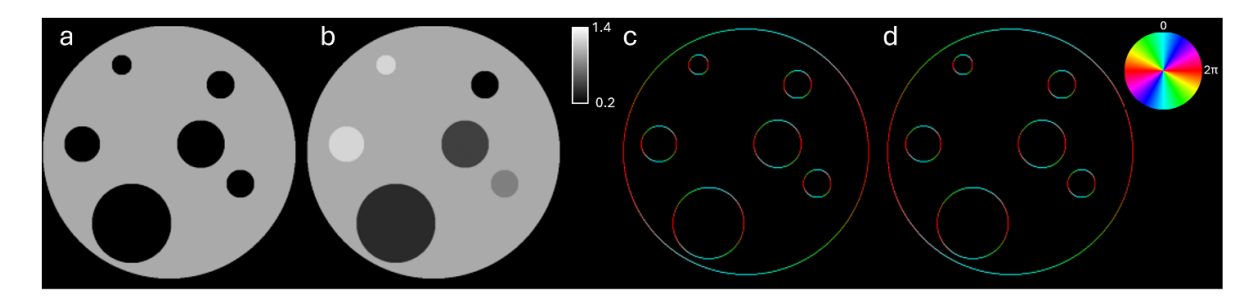


Figure 1. Numerical example showing a slice through an initial volume (a) that transforms through some dynamic process into a new state (b). The corresponding vectors describing the absolute direction of the image gradients in a and b are illustrated in c and d respectively. The modulo  $2\pi$  direction of the vector is encoded in the image hue, which is described by the corresponding colour wheel. Because of the temporal evolution, the slices through the volume in (a) and (b) appear different, however the mutual information encoded in the normalised gradient directions remains constant.

 $70 \, \mu m \times 70 \, \mu m$  and a detector with line spread function (LSF) of  $\sim 30 \, \mu m$ ,  $M_{\rm opt}$  according to equation (3) is 1.43 and thus  $R_2$  was set to 140 mm (resulting in  $R_1 = 320 \, \text{mm}$ ). This geometry resulted in an effective pixel size at the sample plane of  $10.5 \, \mu m$ .

Water uptake in a thin birch wood skewer was used as a dynamic process to test the system. This process involves the filling of vessels in the wood via capillary action, in analogy to the uptake of water and nutrients in living plants. This process does not impact the overall structure or shape of the sample, thus making it a good candidate for reconstruction using a structure-based prior.

A high-quality reference scan was acquired using 1001 projections of 1 s equally distributed through 360°. Dark and flat frame corrected projections were retrieved using the TIEbased equation (4). Due to the polychromatic x-ray source and the complex chemical structure of the wood, determining the correct  $\frac{\delta}{\beta}$  ratio for retrieval is an ambiguous task. In such circumstances, it is commonplace to empirically determine  $\frac{\delta}{\beta}$ [39, 49, 50]. This process generally entails using an approximation of the material composition as a starting point, before manually adjusting to find the value that removes fringes and reduces noise, without over smoothing the image. Using cellulose at 1.5 g cm<sup>-3</sup> density as an approximation for the wood, we find  $\frac{\delta}{\beta} = 1896$  at 19 keV, from tabulated values. We note however that the wood is highly porous below the resolution of the system (see figures 6(e) and (f), and thus this density should be taken as an upper bound estimate. This value was used as an order of magnitude starting point, which was heuristically refined to  $\frac{\delta}{\beta} = 1000$  by visual inspection. The high-quality reference volume v was reconstructed analytically using the FDK algorithm implemented in the core imaging library (CIL) [42].

The dynamic scans were acquired under continuous sample rotation at an angular velocity of  $20^{\circ}$  s<sup>-1</sup>, with the detector operating in continuous acquisition mode with an exposure time of 50 ms. While this was simple to implement, a fast triggered step-and-shoot scan may be required to avoid motion blur with more complex samples. Projections were retrieved using the same parameters as for the high-quality reference scan. Reconstruction from each set of 180 projections results in a temporal resolution of 9 s per full CT scan. While the temporal resolution is set by the time required to acquire an

adequately sampled dataset, if required, the temporal sampling can be increased by using a sliding window reconstruction method [17, 51].

To effectively utilise the dTV regularisation, it is vital that the reference scan v is well aligned with the dynamic data. As the dynamic scan was operated in a flyscan mode, it was necessary to find the angular offset between the start angle of the two scans to ensure alignment of the reconstructions. This was accomplished by minimising the  $l^2$  norm between v and u(t), across some range of angular offsets (see supplementary material 1). A number of frames (16) were skipped by the detector around the midway point of the scan, leading to a change in the offset. Thus the alignment step was taken for each u(t) to ensure consistent alignment with v across all t. A similar process was also used to estimate the correct angular step between projections, to account for the finite detector readout and dead time (see supplementary material 2).

Reconstruction of the dynamic data was accomplished by solving equation (6) using the PDHG method in CIL [35, 42] for each time step t. For each t, u(t) was initialised with an FDK reconstruction  $u_{\rm FDK}(t)$  to speed convergence, followed by 10 PDHG iterations with  $\alpha = 5 \times 10^{-9}$  and edge parameter  $\eta = 5 \times 10^{-11}$ , both chosen by visual inspection to optimise the CNR. We will present reconstructions acquired by direct analytic reconstruction of attenuation data, direct analytic reconstruction of phase-retrieved data, and dTV regularised reconstruction of phase-retrieved data, which will be henceforth referred to as conventional, analytical phase-retrieved, and regularised phase-retrieved respectively.

### 3. Results and discussion

# 3.1. Demonstration of phase-contrast edge enhancement

To demonstrate the potential of FSP XPCI using the lab-based system, the same birch skewer sample was imaged with  $R_2 = 140$  mm, and compared to the equivalent contact image with  $R_2 \approx 0$  mm, resulting in effective pixel sizes of 10.5  $\mu$ m and 15  $\mu$ m respectively. We note that despite the increased magnification, source induced blur results in a very similar spatial resolution between the two cases, of 29.7  $\mu$ m and 30.0  $\mu$ m respectively, according to equation (2). Despite this, much

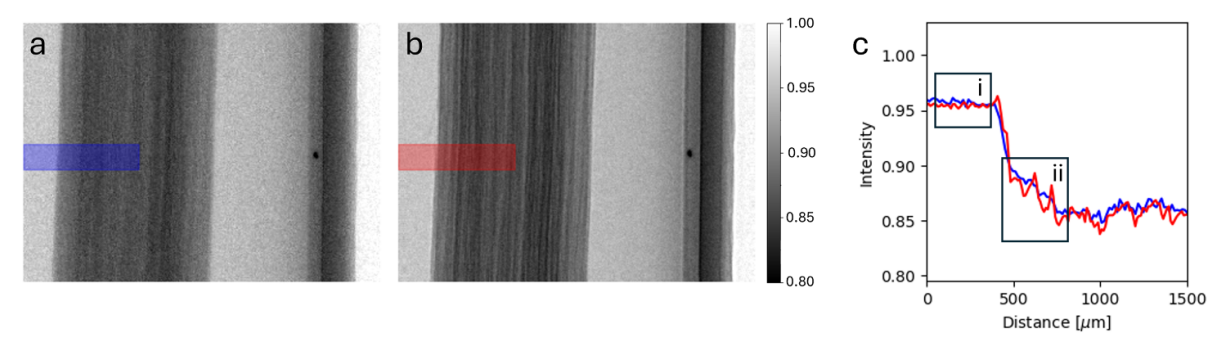
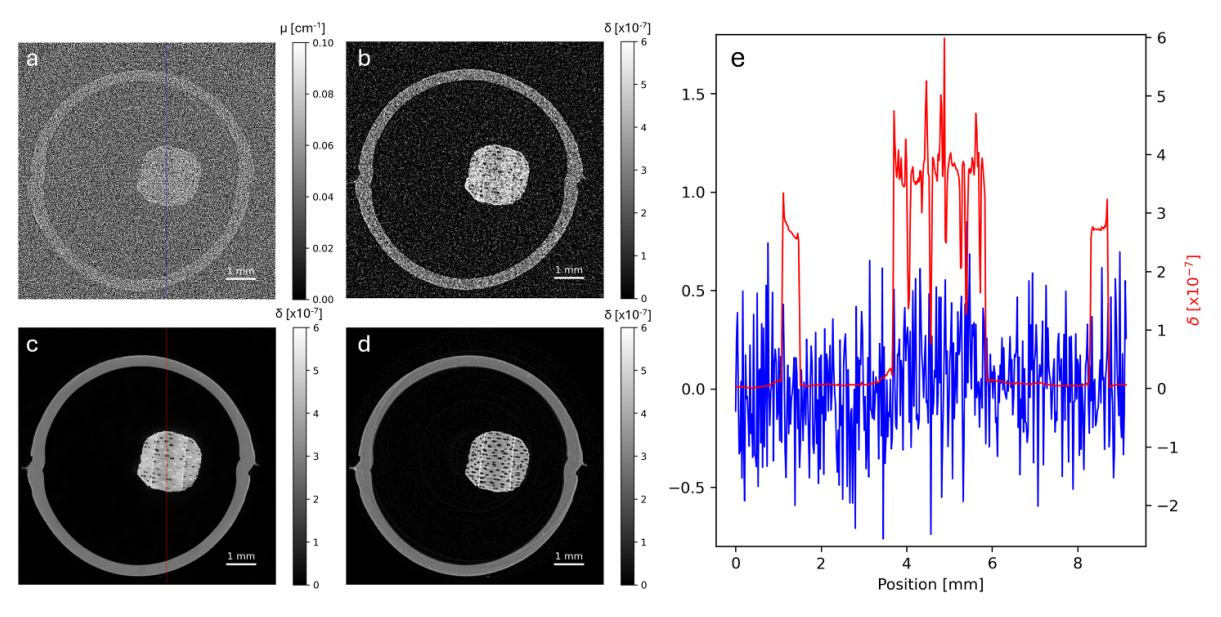


Figure 2. Comparison of the same birch wood skewer imaged with a propagation distance of  $R_2 \approx 0$  mm (a) and  $R_2 = 140$  mm (b). Plotted line profiles (c) illustrate increased structure and phase fringes at the sample edges. We highlight how despite similar noise levels in the background (ci), the signal features much larger oscillations (cii) due to phase effects in b. Both images are the average of  $5 \times 3$  s exposures, indicating an increase in feature visibility at the same exposure.



**Figure 3.** Axial slices of the reconstructed wooden skewer during the 9s temporal resolution dynamic scan, conventional (a), analytical phase-retrieved (b), and regularised phase-retrieved (c). Axial slice of the high-quality reference reconstruction, which was used as a structure-based prior for the regularisation (d). Line profiles (e) from the slices in (a) and (c) demonstrate the much greater CNR of the regularised phase-retrieved reconstruction, despite using the same raw data as the conventional reconstruction.

more structure is visible in the wood in the FSP image in figure 2(b) compared to the contact image in figure 2(a). The line profiles plotted in figure 2(c) show clear edge enhancement in regions of the skewer that appear relatively homogenous in the contact image. It is important to note that both images were obtained from the average of  $5 \times 3$  s exposures acquired with the same source-to-detector distance, with the only difference being the propagation distance  $R_2$ . Phase effects and edge enhancement were therefore obtained without any loss of flux or change in the acquisition process, thus making FSP XPCI an efficient method for dynamic imaging.

#### 3.2. Effect of phase-retrieval and regularised reconstruction

Figure 3 shows the same axial slice of the conventional 3(a), analytical phase-retrieved 3(b), and regularised phase-retrieved 3(c) reconstructions. All slices were reconstructed

using the same 9s of input data, immediately after beginning dynamic micro-CT acquisition. Figure 3(d) shows the same axial slice of the same sample in a dry state, before initiating the dynamic experiment. This was reconstructed from ~16 min of well sampled data, providing a high-quality reconstruction to act as a structure-based prior for dTV regularisation. Line profiles plotted in figure 3(e) corresponding to the conventional and the regularised phase-retrieved reconstruction illustrate the much superior CNR achieved using the same dataset with appropriate data processing and advanced reconstruction methods. In figure 3(a), only the approximate shape of the sample can be made out, with no structure visible. In figure 3(b), after phase-retrieval, the structure of the vessels start to appear but are largely obscured by noise. Finally, in figure 3(c), the air filled vessels are well delineated from the wood, and the water filled vessels now become visible.

To demonstrate quantitatively the practical impact of the phase-retrieval and regularised reconstruction, figure 4(a)

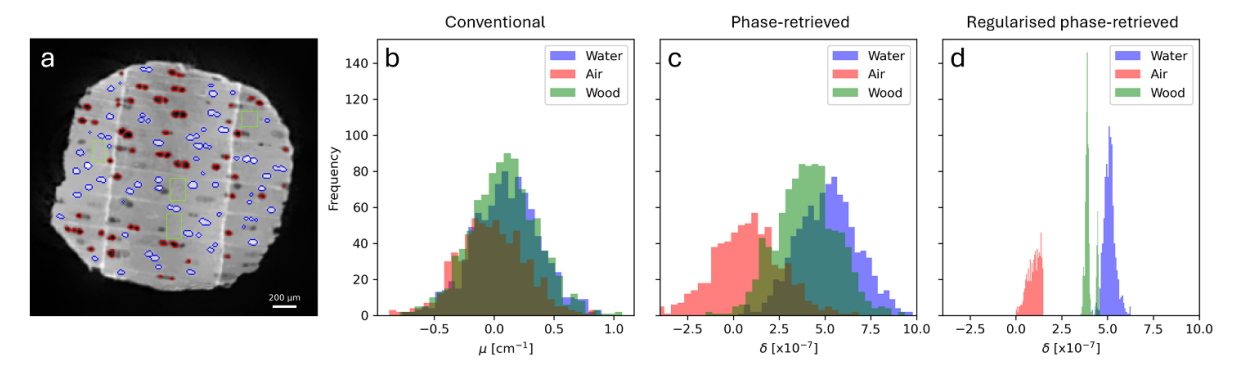


**Figure 4.** Segmented axial slice of the regularised phase-retrieved reconstruction (a). Red-bordered regions indicate unfilled vessels, while blue-bordered regions indicate water filled vessels. The green rectangles indicate regions of the wood used to measure the distribution of grey-values. Histograms of voxels falling into the water, air, or wood categories are shown for the conventional (b), the analytical phase-retrieved (c), and the regularised phase-retrieved reconstruction (d).

**Table 1.** Comparison of conventional, analytical phase-retrieved, and regularised phase-retrieved grey-values (mean  $\pm$  standard deviation) for each material category. The  $\mu$  values represent the reconstructed linear attenuation coefficient, while the  $\delta$  values represent the unitless real part of the complex refractive index. Care should be taken in the interpretation of the  $\delta$  values, which are non-quantitative due to the assumptions of the phase-retrieval method.

Material	Conventional $\mu$ (cm <sup>-1</sup> )	Analytical PR $\delta [\times 10^{-7}]$	Regularised PR $\delta$ [×10 <sup>-7</sup> ]
Air	$-0.02 \pm 0.28$	$0.81 \pm 1.85$	$0.97 \pm 0.35$
Birch	$0.08 \pm 0.28$	$4.00\pm1.65$	$3.98 \pm 0.24$
Water	$0.10\pm0.28$	$5.14 \pm 1.62$	$5.11 \pm 0.31$

shows an axial slice complete with an overlaid segmentation of air-filled and water-filled vessels. Some of the vessels feature intermediate grey-values (and are thus excluded from the following analysis), indicating that the waterfront reached this vertical position during the finite acquisition time of this time point. Using the segmented vessel voxels and the representative wood regions indicated on figure 4(a) by the green rectangles, histograms of each category were computed for each of the reconstructed slices. With each additional processing step, moving from figures 4(b)-(d), it is seen that the grey-values belonging to each category become more separated. The mean values and standard deviations of voxels categorised as air, birch, and water are tabulated in table 1. Care should be taken in the interpretation of the  $\delta$  values, which are non-quantitative due to the broken assumptions (multi-material sample, polychromatic source) of the phase-retrieval method. We note how the increasing separation of the histograms is also reflected in the decrease in the relative size of the standard deviations in table 1.

Both the analytical and regularised reconstructions of the phase-retrieved data yield comparable grey-values. This is particularly insightful for the reconstruction of the water, indicating that the reconstruction does not become biased when regularised by a reference which did not contain water. Having initially segmented vessels using the high-quality reference volume, it is important for further analysis that voxels within

the vessels can subsequently be accurately categorised as water or air. To enable a direct comparison of each method (despite the change in units), the CNR of water compared to air was calculated, where CNR =  $(water - air)/\sigma$ , with  $\sigma$  defined as the mean standard deviation of the two categories. These calculations were made using the tabulated values in table 1, extracted from the regions indicated on figure 4. The resultant CNR<sub>conv</sub> = 0.43, CNR<sub>PR</sub> = 2.50, and CNR<sub>PRreg</sub> = 12.55 indicate the much improved category separation after phase-retrieval (a factor of 5.8x) and after regularised reconstruction (a factor of 29.2x).

# 3.3. Spatial resolution

Figure 5(a) shows a coronal slice of the volume u(t = 9 s)reconstructed using the regularised phase-retrieval method. To characterise the spatial resolution of the reconstructions, edge response functions (ERFs) were taken at a number of locations. From each of these, the Gaussian equivalent full-width-at-half-maximums (FWHMs) were calculated. An ERF taken at a vessel edge represents a static region of the sample, in which no water transport has yet occurred, and thus the gradients of v and u(t = 9 s) are very well aligned. A zoom of this region is shown for the regularised phase-retrieved volume 5(b) and the analytical phase-retrieved volume 5(e). Both the regularised (29.0 µm) and analytical (30.8 µm) reconstructions yielded FWHMs consistent with the 29.7 µm system resolution estimated using equation (2). Another location examined the dynamically changing water level 5(c) and (f), as here the gradients of v and u(t = 9 s)are no longer parallel. In fact, the total lack of gradient in v at this location causes the regularisation term to penalise anything but flat structure in this region. While motion blur already slightly reduces the resolution of the analytical phaseretrieved volume (70.0 μm), the regularised phase-retrieved result is severely reduced (204.9 µm). We note that the motion blur component here could be reduced by faster scanning, highlighting the correlation between temporal and spatial resolution. A final region examined the static water-wood interface 5(d) and (g). Despite the change of interface materials from those in v, the image gradients are still parallel, and

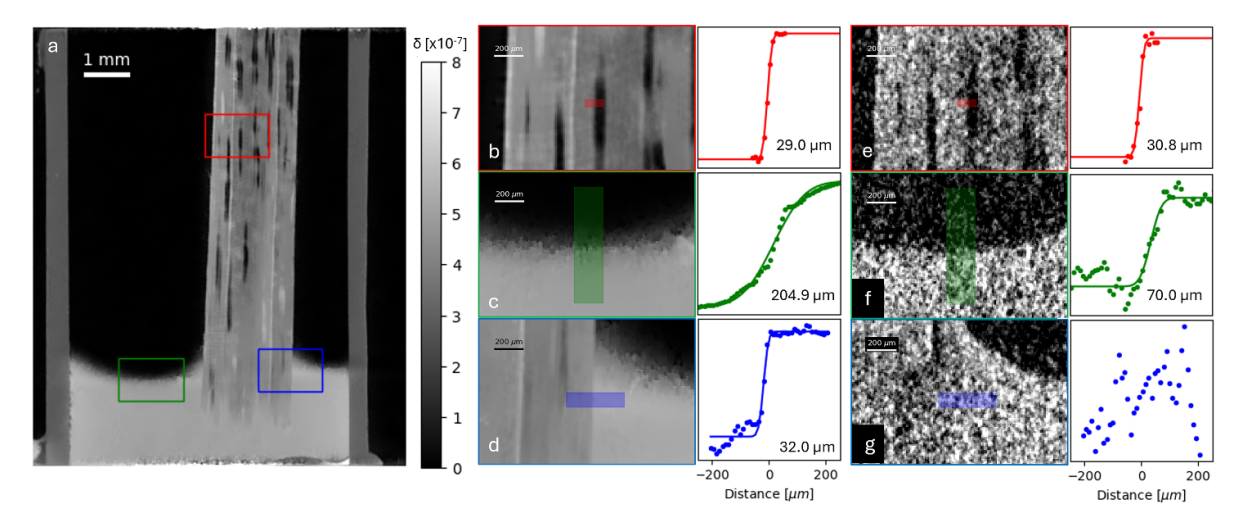


**Figure 5.** A coronal slice of the regularised phase-retrieved volume u(t = 9 s). Zoomed regions are indicated on the figure, illustrating static air-filled structures within the skewer (b), the dynamically changing water level within the container (c), and the static wood-water interface (d). Panels, (e), (f), and (g) respectively show the corresponding zooms from the analytical phase-retrieved volume. Each panel is accompanied by the extracted edge response function at the position indicated by the coloured blocks. The highest spatial-resolution is observed in the static case, where both the analytical (e) and regularised (b) results matched the theoretical resolution of the imaging system. Regularisation vastly improves on the CNR of dynamic regions (c), however with a threefold compromise on the achieved spatial resolution.

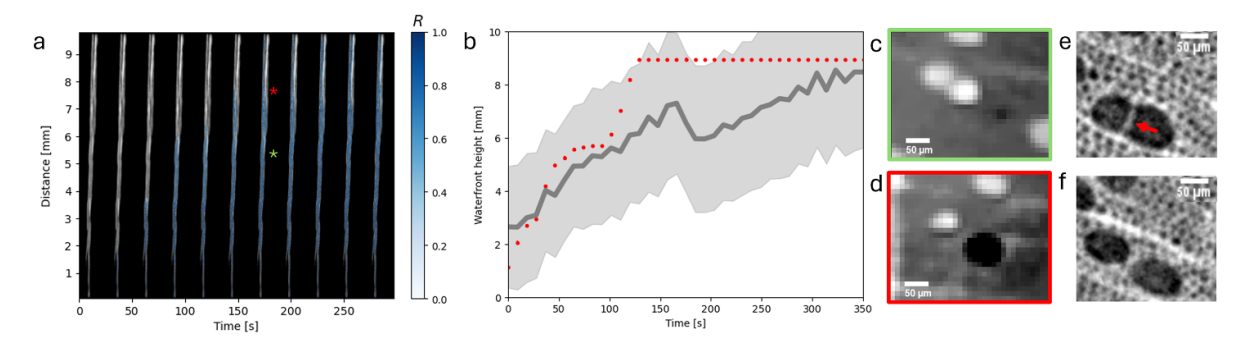


**Figure 6.** The progression of water up a single vessel of the skewer is visualised throughout the duration of the scan (a). The ratio *R* of water thickness to total vessel thickness is overlaid in blue at intervals of 27 s. The progression of the waterfront in the vessel shown in (a) is plotted with red markers in (b), error bars are included but are smaller than the markers. In dark grey is the median waterfront height, while the light grey filled region indicates the standard deviation across all vessels. A sharp jump in the waterfront height at around 100 s corresponds to the branching from joined vessels (c), into separated vessels (d). The approximate locations of (c) and (d) are indicated by the colour matched asterisks on (a). A higher resolution scan of a similar sample shows the structure in greater detail, where two vessels are joined by a thin membrane (e), but later separate to become independent (f).

thus a resolution of  $32.0\,\mu m$  is retrieved for the regularised phase-retrieved volume, comparable to the static case. The very low CNR of the water-wood interface in the analytical phase-retrieved image precluded the extraction of a reasonable ERF, further highlighting the impressive gains in the regularised reconstruction.

While the spatial resolution loss on the dynamic water level region indicates a potential limitation of the method, we emphasise that this impacts only the region of the reconstruction in which the reference and target gradients are not parallel. Figure 5(d) highlights how the parallel gradients enforce accurate reconstruction of the vessels, with crisp interfaces, despite the filling of the vessel with a new material.

# 3.4. Capillary uptake of water in birch vessels

The progression of the waterfront up the skewer was characterised for each vessel independently. Voxels within the vessels were classified as containing water when the difference in voxel grey-value  $\delta_{u(t)}$ — $\delta_v$  was greater than the halfway point between the classes,  $(\bar{\delta}_{\text{water}} - \bar{\delta}_{\text{air}})/2 = 2.07 \times 10^{-7}$ . Following this, R was calculated as the ratio of the projected thickness in the coronal plane of water containing voxels to the projected thickness of the vessel. The progression of the waterfront up the skewer is visualised for a single vessel in figure 6(a).

The waterfront height in a given vessel was subsequently extracted by finding the height at which the total ratio of water

to vessel thickness drops below 0.1, and remains below this threshold for a distance of 20 pixels (210 µm). The evolution of the waterfront height in the vessel in figure 6(a) is plotted with red markers in figure 6(b). Note that error bars were calculated by varying the ratio threshold between 0.05 and 0.15, but are smaller than the markers and thus are not visible. The small measurement error can be explained by the extraction of the 1D metric R from the sum of many voxels across the vessel cross section, as well as the 20 pixel persistence threshold suppressing noise due to air inclusions or rogue water droplets. The dark grey line on the same plot indicates the median waterfront height across all vessels, while the light grey filled region indicates the standard deviation across all vessels. A large part of the variance in waterfront height across vessels comes from differences in the initiation time of water entering a given vessel, as well as branching structures causing an uneven flow rate for some vessels.

In particular, the individually plotted vessel shows a sharp jump in waterfront height at around 100 s. Closer examination in figure 6(c) shows that this corresponds to the water flow shifting from movement through a joined vessel pair, which then separates, with the water only continuing to move in a single vessel, illustrated in figure 6(d). Figure 6(e) and (f) illustrate this structure in a higher resolution scan (see supplementary material 3) of a similar sample. Initially, two vessels are connected by a thin membrane, through which water may permeate allowing joint movement of the waterfront through a large effective vessel diameter. These vessels then separate, and it is possible that water may continue to flow through only one vessel, taking the path of least resistance. As the capillary rise is inversely proportional to the vessel radius, this results in a rapid advancement of the waterfront height. There are indications that the exact grouping of vessels within a network are an adaption to reduce the risk of embolism [52, 53], allowing fluids to continue undisrupted through interconnected vessels even in the presence of obstructions. This suggests that our methodology may be suitable for the measurement and monitoring of such processes, providing time-resolved insights at the microscale.

We applied our system and methodology to the measurement of water flow through a wooden skewer via capillary action, which was chosen as representative of a class of experiments in the study of fluid transport. In particular, the method proposed here could be applied to the measurement of water flow in and around plants using both x-ray [54, 55] and neutron tomography [56, 57]. Similarly, the measurement of fluid flow through multi-phase materials and pore networks is an active research area for which the structural similarity of image features throughout the course of a scan could be leveraged to improve CNR [18, 58, 59].

Potential clinical uses for the methodology include estimation of blood flow or airflow in animal models of health and disease [60–62]. Labelled radiodense particles could for example be used to measure flow perturbation at different severities of tissue damage in various organs of interest. In the pharmacological domain, such methods could also be used to estimate the distribution and mechanics of inhaled substances in the airways following deposition of therapeutic compounds,

as has been demonstrated using radiography [63, 64]. This could help determine whether active molecules are reaching their desired target location, as well as providing an experimental framework with which to optimise drug delivery using aerosol or nebulised routes of administration.

In applications such as in-vivo biological imaging where larger sample structure change is encountered, a single reference scan would not be sufficient to capture the expected image gradients. In such cases, the demonstrated improvement in CNR associated with phase-retrieval would be an important advantage. Alternatively, future work could investigate other reconstruction methods based on mutual information shared between time-points [34], without utilising a high-quality reference.

#### 4. Conclusion

We have presented an experimental setup and data processing methodology for dynamic x-ray phase-contrast microtomography on the seconds timescale with a compact setup. The use of a detector with sufficient spatial resolution to resolve phase fringes, in conjunction with phase-retrieval, allowed substantial (5.8x) improvements in the CNR. This was based on FSP of the x-ray beam and did not require additional optical elements, with the benefit of exploiting all of the available flux. The absence of optical elements simplifies the data acquisition by removing potential constraints linked to their alignment or stepping. Furthermore, we have shown iterative reconstruction using structure-based dTV regularisation. The combination of these two techniques generated a notable increase in the contrast to noise ratio of ~29x, allowing accurate segmentation and classification of voxels despite the relatively fast exposures. We demonstrated that in regions where the gradients of the reference and dynamic reconstruction are aligned, the achievable spatial resolution is consistent with theoretical predictions, despite using undersampled data. We envisage a range of potential applications for the demonstrated approach, including, for example plant research, pore-scale flow experiments, and flow estimation in animal models.

# Data availability statement

The data cannot be made publicly available upon publication because they are not available in a format that is sufficiently accessible or reusable by other researchers. The data that support the findings of this study are available upon reasonable request from the authors.

### **Acknowledgments**

This work is supported by the EPSRC-funded UCL Centre for Doctoral Training in Intelligent, Integrated Imaging in Healthcare (i4health) (EP/S021930/1), the Department of Healths NIHR funded Biomedical Research Centre at University College London Hospitals, and the National Research Facility for Lab x-ray CT (NXCT) through EPSRC Grants EP/T02593X/1 and EP/V035932/1; and by the

Wellcome Trust 221367/Z/20/Z. This work is also supported by the Francis Crick Institute, which receives its core funding from Cancer Research UK (CC0102), the UK Medical Research Council (CC0102), and the Wellcome Trust (CC0102).

#### **ORCID iDs**

Harry Allan © 0000-0002-7891-9346 Tom Partridge © 0000-0001-8135-2099 Marco Endrizzi © 0000-0002-7810-2301

#### References

- [1] Withers P J, Bouman C, Carmignato S, Cnudde V, Grimaldi D, Hagen C K, Maire E, Manley M, Plessis A D and Stock S R 2025 X-ray computed tomography *Nat. Rev. Methods* Primers 1 18
- [2] Marone F, Schlepütz C M, Marti S, Fusseis F, Velásquez-Parra A, Griffa M, Jiménez-Martínez J, Dobson K J and Stampanoni M 2020 Time resolved in situ x-ray tomographic microscopy unraveling dynamic processes in geologic systems Front. Earth Sci. 7 346
- [3] Babin P, Valle G D, Chiron H, Cloetens P, Hoszowska J, Pernot P, Réguerre A, Salvo L and Dendievel R 2006 Fast x-ray tomography analysis of bubble growth and foam setting during breadmaking J. Cereal Sci. 43 393–7
- [4] Mokso R, Marone F, Haberthür D, Schittny J, Mikuljan G, Isenegger A and Stampanoni M 2011 Following dynamic processes by x-ray tomographic microscopy with sub-second temporal resolution AIP Conf. Proc. 1365 38–41
- [5] Thompson A, Maskery I and Leach R K 2016 X-ray computed tomography for additive manufacturing: a review *Meas. Sci. Technol.* 27 072001
- [6] Du Plessis A, Yadroitsev I, Yadroitsava I and Le Roux S G 2018 X-ray microcomputed tomography in additive manufacturing: a review of the current technology and applications 3D Print. Addit. Manuf. 5 227–47
- [7] Murrie R P *et al* 2020 Real-time *in vivo* imaging of regional lung function in a mouse model of cystic fibrosis on a laboratory X-ray source *Sci. Rep.* **10** 447
- [8] Fardin L, Broche L, Lovric G, Mittone A, Stephanov O, Larsson A, Bravin A and Bayat S 2021 Imaging atelectrauma in ventilator-induced lung injury using 4D x-ray microscopy Sci. Rep. 11 4236
- [9] Walker S M, Schwyn D A, Mokso R, Wicklein M, Müller T, Doube M, Stampanoni M, Krapp H G and Taylor G K 2014 In vivo time-resolved microtomography reveals the mechanics of the blowfly flight motor PLOS Biol. 12 e1001823
- [10] Endrizzi M 2018 X-ray phase-contrast imaging Nucl. Instrum. Methods Phys. Res. A 878 88–98
- [11] Kitchen M J, Buckley G A, Gureyev T E, Wallace M J, Andres-Thio N, Uesugi K, Yagi N and Hooper S B 2017 CT dose reduction factors in the thousands using x-ray phase contrast Sci. Rep. 7 15953
- [12] Mokso R *et al* 2017 Gigafrost: the gigabit fast readout system for tomography *J. Synchrotron Radiat.* **24** 1250–9
- [13] Yashiro W, Noda D and Kajiwara K 2017 Sub-10-ms x-ray tomography using a grating interferometer Appl. Phys. Express 10 052501
- [14] García-Moreno F, Kamm P H, Neu T R, Bülk F, Mokso R, Schlepütz C M, Stampanoni M and Banhart J 2019 Using x-ray tomoscopy to explore the dynamics of foaming metal Nat. Commun. 10 3762

- [15] Zwanenburg E, Williams M and Warnett J M 2021 Review of high-speed imaging with lab-based x-ray computed tomography Meas. Sci. Technol. 33 012003
- [16] Eggert A, Müller M, Nachtrab F, Dombrowski J, Rack A and Zabler S 2014 High-speed in-situ tomography of liquid protein foams *Int. J. Mater. Res.* 105 632–9
- [17] Dewanckele J, Boone M, Coppens F, Van Loo D and Merkle A 2020 Innovations in laboratory-based dynamic micro-CT to accelerate in situ research J. Microsc. 277 197–209
- [18] Bultreys T, Boone M A, Boone M N, De Schryver T, Masschaele B, Van Hoorebeke L and Cnudde V 2016 Fast laboratory-based micro-computed tomography for pore-scale research: illustrative experiments and perspectives on the future Adv. Water Resour. 95 341–51
- [19] Vavřík D, Jakubek J, Kumpová I and Pichotka M 2017 Laboratory-based study of dynamical processes by 4D x-ray CT with sub-second temporal resolution *J. Instrum.* 12 C02010
- [20] Mäkiharju S A, Dewanckele J, Boone M, Wagner C and Griesserr A 2022 Tomographic x-ray particle tracking velocimetry: proof-of-concept in a creeping flow *Exp. Fluids* 63 1–12
- [21] Allan H, Navarrete-Leon C, Roche i Morgó O, Jia Y and Endrizzi M 2024 Sub-second dynamic x-ray micro-CT and fast phase-sensitive multi-contrast micro-CT with a laboratory source *Proc. SPIE* 13152 1315200
- [22] Parker J T, Dreier T, Nilsson D and Mäkiharju S A 2024 In-lab x-ray particle velocimetry for multiphase flows: design principles and demonstration of O(1 kHz) XPV Flow Meas. Instrum. 96 102536
- [23] Pfeiffer F, Weitkamp T, Bunk O and David C 2006 Phase retrieval and differential phase-contrast imaging with low-brilliance x-ray sources Nat. Phys. 2 258–61
- [24] Olivo A and Speller R 2007 A coded-aperture technique allowing x-ray phase contrast imaging with conventional sources Appl. Phys. Lett. 91 074106
- [25] Vittoria F A, Kallon G K, Basta D, Diemoz P C, Robinson I K, Olivo A and Endrizzi M 2015 Beam tracking approach for single–shot retrieval of absorption, refraction and dark–field signals with laboratory x–ray sources App. Phys. Lett. 106 224102
- [26] Zanette I, Zhou T, Burvall A, Lundström U, Larsson D H, Zdora M, Thibault P, Pfeiffer F and Hertz H M 2014 Speckle-based x-ray phase-contrast and dark-field imaging with a laboratory source *Phys. Rev. Lett.* 112 253903
- [27] John D, Gottwald W, Berthe D, Wirtensohn S, Hickler J, Heck L and Herzen J 2024 X-ray dark-field computed tomography for monitoring of tissue freezing Sci. Rep. 14 5599
- [28] Massimi L, Clark S J, Marussi S, Doherty A, Schulz J, Marathe S, Rau C, Endrizzi M, Lee P D and Olivo A 2021 Dynamic multicontrast x-ray imaging method applied to additive manufacturing *Phys. Rev. Lett.* 127 215503
- [29] Wilkins S W, Gureyev T E, Gao D, Pogany A and Stevenson A W 1996 Phase-contrast imaging using polychromatic hard x-rays *Nature* 384 335–8
- [30] Gradl R et al 2018 In vivo dynamic phase-contrast X-ray imaging using a compact light source Sci. Rep. 8 6882
- [31] Beister M, Kolditz D and Kalender W A 2012 Iterative reconstruction methods in x-ray CT *Phys. Med.* **28** 94–108
- [32] Gilbert P 1972 Iterative methods for the three-dimensional reconstruction of an object from projections *J. Theor. Biol.* **36** 105–17
- [33] Hendriksen A A, Pelt D M and Batenburg K J 2020 Noise2inverse: self-supervised deep convolutional denoising for tomography *IEEE Trans. Comput. Imaging* 6 1320–35
- [34] Ritschl L, Sawall S, Knaup M, Hess A and Kachelrieß M 2012 Iterative 4D cardiac micro-CT image reconstruction using

- an adaptive spatio-temporal sparsity prior *Phys. Med. Biol.* **57** 1517
- [35] Papoutsellis E et al 2021 Core imaging library-part II: multichannel reconstruction for dynamic and spectral tomography Phil. Trans. R. Soc. A 379 20200193
- [36] Paganin D 2006 Coherent X-ray Optics (Oxford University Press) No. 6
- [37] Bidola P M, Zanette I, Achterhold K, Holzner C and Pfeiffer F 2015 Optimization of propagation-based phase-contrast imaging at a laboratory setup *Opt. Express* 23 30000–13
- [38] Lioliou G, Buchanan I, Astolfo A, Endrizzi M, Bate D, Hagen C and Olivo A 2024 Framework to optimize fixed-length micro-CT systems for propagation-based phase-contrast imaging *Opt. Express* 32 4839–56
- [39] Eckermann M, Töpperwien M, Robisch A-L, van der Meer F, Stadelmann C and Salditt T 2020 Phase-contrast x-ray tomography of neuronal tissue at laboratory sources with submicron resolution J. Med. Imaging 7 013502
- [40] Esposito M, Schieber N, Olivo A, Schwab Y and Endrizzi M 2025 Laboratory-based x-ray phase contrast microscopy system for targeting in unstained soft-tissue samples *Phys. Rev. Res.* 7 013037
- [41] Paganin D, Mayo S C, Gureyev T E, Miller P R and Wilkins S W 2002 Simultaneous phase and amplitude extraction from a single defocused image of a homogeneous object J. Microsc. 206 33–40
- [42] Jørgensen J S *et. al.* 2021 Core imaging library-part I: a versatile Python framework for tomographic imaging *Phil. Trans. R. Soc A* **379** 20200192
- [43] Feldkamp L A, Davis L C and Kress J W 1984 Practical cone-beam algorithm *J. Opt. Soc. Am. A* 1 612–9
- [44] Chen G-H, Tang J and Leng S 2008 Prior image constrained compressed sensing (PICCS): a method to accurately reconstruct dynamic CT images from highly undersampled projection data sets *Med. Phys.* 35 660–3
- [45] Myers G R, Kingston A M, Varslot T K, Turner M L and Sheppard A P 2011 Dynamic tomography with a *priori* information *Appl. Opt.* 50 3685–90
- [46] Kazantsev D, Ourselin S, Hutton B F, Dobson K J, Kaestner A P, Lionheart W R, Withers P J, Lee P D and Arridge S R 2014 A novel technique to incorporate structural prior information into multi-modal tomographic reconstruction *Inverse Problems* 30 065004
- [47] Ehrhardt M J and Arridge S R 2013 Vector-valued image processing by parallel level sets *IEEE Trans. Image Process.* 23 9–18
- [48] Roche i Morgó O, Jia Y, Allan H, Doherty A, Navarrete-León C, Astolfo A, Jiang L, Ferrara J D and Endrizzi M 2024 A new user facility with flexible multi-scale, multi-contrast micro-CT capabilities *Proc.* SPIE 13152 1315209
- [49] Brombal L et. al. 2019 Monochromatic propagation-based phase-contrast microscale computed-tomography system with a rotating-anode source Phys. Rev. Appl. 11 034004

- [50] Weitkamp T, Haas D, Wegrzynek D and Rack A 2011 ANKAphase: software for single-distance phase retrieval from inline x-ray phase-contrast radiographs J. Synchrotron Radiat. 18 617–29
- [51] Bultreys T, Boone M A, Boone M N, De Schryver T, Masschaele B, Van Loo D, Van Hoorebeke L and Cnudde V 2015 Real-time visualization of H aines jumps in sandstone with laboratory-based microcomputed tomography Water Resour. Res. 51 8668–76
- [52] Carlquist S 1984 Vessel grouping in dicotyledon wood Aliso 10 505–25
- [53] Mrad A, Domec J-C, Huang C-W, Lens F and Katul G 2018 A network model links wood anatomy to xylem tissue hydraulic behaviour and vulnerability to cavitation *Plant Cell Environ.* 41 2718–30
- [54] Kim H K and Lee S J 2010 Synchrotron x-ray imaging for nondestructive monitoring of sap flow dynamics through xylem vessel elements in rice leaves *New Phytol*. 188 1085–98
- [55] Daly K R, Tracy S R, Crout N M, Mairhofer S, Pridmore T P, Mooney S J and Roose T 2018 Quantification of root water uptake in soil using x-ray computed tomography and image-based modelling *Plant Cell Environ.* 41 121–33
- [56] Warren J M, Bilheux H, Kang M, Voisin S, Cheng C-L, Horita J and Perfect E 2013 Neutron imaging reveals internal plant water dynamics *Plant Soil* 366 683–93
- [57] Tötzke C, Kardjilov N, Manke I and Oswald S E 2017 Capturing 3D water flow in rooted soil by ultra-fast neutron tomography Sci. Rep. 7 6192
- [58] Menke H P, Bijeljic B, Andrew M G and Blunt M J 2015 Dynamic three-dimensional pore-scale imaging of reaction in a carbonate at reservoir conditions *Environ. Sci. Technol.* 49 4407–14
- [59] Andrew M, Menke H, Blunt M J and Bijeljic B 2015 The imaging of dynamic multiphase fluid flow using synchrotron-based x-ray microtomography at reservoir conditions *Transp. Porous Med.* 110 1–24
- [60] Jung S Y, Ahn S, Nam K H, Lee J P and Lee S J 2012 *In vivo* measurements of blood flow in a rat using x-ray imaging technique *Int. J. Cardiovasc. Imaging* 28 1853–8
- [61] Park H, Yeom E and Lee S J 2016 x-ray PIV measurement of blood flow in deep vessels of a rat: an *in vivo* feasibility study *Sci. Rep.* **6** 19194
- [62] Asosingh K, Frimel M, Zlojutro V, Grant D, Stephens O, Wenger D, Fouras A, DiFilippo F and Erzurum S 2022 Preclinical four-dimensional functional lung imaging and quantification of regional airflow: a new standard in lung function evaluation in murine models Am. J. Respir. Cell Mol. Biol. 67 423–9
- [63] Gradl R et. al. 2019 Visualizing treatment delivery and deposition in mouse lungs using in vivo x-ray imaging J. Control. Release 307 282–91
- [64] Donnelley M, Morgan K S, Siu K K and Parsons D W 2013 Variability of in vivo fluid dose distribution in mouse airways is visualized by high-speed synchrotron x-ray imaging J. Aerosol Med. Pulm. Drug Deliv. 26 307–16